Dynamic nucleosome remodeling mediated by YY1 underlies early mouse development

Mizuki Sakamoto,[1,4] Shusaku Abe,[2,4] Yuka Miki,[2] Yusuke Miyanari,[3] Hiroyuki Sasaki,[2] and Takashi Ishiuchi[1]

[1]Faculty of Life and Environmental Sciences, University of Yamanashi, Yamanashi 400-8510, Japan; [2]Division of Epigenomics and Development, Medical Institute of Bioregulation, Kyushu University, Fukuoka 812-8582, Japan; [3]NanoLSI, Cancer Research Institute, Kanazawa University, Kanazawa 920-1192, Japan

Nucleosome positioning can alter the accessibility of DNA-binding proteins to their cognate DNA elements, and thus its precise control is essential for cell identity and function. Mammalian preimplantation embryos undergo temporal changes in gene expression and cell potency, suggesting the involvement of dynamic epigenetic control during this developmental phase. However, the dynamics of nucleosome organization during early development are poorly understood. In this study, using a low-input MNase-seq method, we show that nucleosome positioning is globally obscure in zygotes but becomes well defined during subsequent development. Down-regulation of the chromatin assembly in embryonic stem cells can partially reverse nucleosome organization into a zygote-like pattern, suggesting a possible link between the chromatin assembly pathway and fuzzy nucleosomes in zygotes. We also reveal that YY1, a zinc finger-containing transcription factor expressed upon zygotic genome activation, regulates the de novo formation of well-positioned nucleosome arrays at the regulatory elements through identifying YY1-binding sites in eight-cell embryos. The YY1-binding regions acquire H3K27ac enrichment around the eight-cell and morula stages, and YY1 depletion impairs the morula-to-blastocyst transition. Thus, our study delineates the remodeling of nucleosome organization and its underlying mechanism during early mouse development.

Nucleosomes are the basic units of chromatin and consist of ~147 bp of DNA wrapped around a core histone octamer composed of histones H2A, H2B, H3, and H4. As nucleosomes themselves limit DNA-templated processes, such as transcription, replication, and repair, their positioning must be precisely regulated such that specific genomic sites can be accessed by regulatory factors at a desired time (Sadeh and Allis 2011; Teves et al. 2014). Nucleosome positioning along genomic DNA is determined by intrinsic DNA sequence, ATP-dependent chromatin remodelers, transcription factors (TFs), and chromatin assembly and disassembly (Lai and Pugh 2017). Certain TFs induce nucleosome remodeling through the recruitment of chromatin remodelers or their intrinsic properties. A subset of TFs, called pioneer TFs, binds to their target sequences on nucleosomal DNA and subsequently creates either an open or closed chromatin environment to control cell fate (Zaret and Mango 2016). TF binding occurs at regulatory elements including promoters and enhancers and facilitates the formation of accessible nucleosome-depleted regions (NDRs) that are often flanked by well-positioned nucleosome arrays (Isbel et al. 2022). For example, NDRs are formed at the transcription start sites (TSSs) of the active genes, and +1 to +5 and −1 well-positioned nucleosomes align downstream from and upstream of the TSSs, respectively. These nucleosomes at the regulatory elements serve as substrates for histone modification and undergo active turnover by histone variants. Therefore, nucleosome positioning is at the basis of epigenetic landscapes.

Recent low-input technologies for profiling epigenetic landscapes have revealed a unique epigenetic status as well as dynamic remodeling in mammalian early embryos (Fu et al. 2020; Xia and Xie 2020; Xu et al. 2021). For example, H3K4me3 shows a noncanonical distribution pattern

in mature mouse oocytes and zygotes, forming unusually broad domains spanning >10 kb. However, the H3K4me3 distribution undergoes a transition from a noncanonical to a canonical pattern at the late two-cell stage through zygotic genome activation (ZGA) (Dahl et al. 2016; Zhang et al. 2016). In mice, major ZGA occurs at the middle to late two-cell stage, whereas minor ZGA starts as early as the late zygote stage, and both serve as signatures of the initiation of the early developmental program (Eckersley-Maslin et al. 2018). There appears to be a permissive chromatin state for ZGA in mouse zygotes, which typically allows the promiscuous transcription of MERVL and other genes (Abe et al. 2015; Wu et al. 2016). Although the requisite of the permissive chromatin state is yet to be understood, the formation of a relaxed chromatin state might be important because high histone mobility, chromatin decompaction, and the absence of DAPI-dense heterochromatic structures are specifically found at these stages (Ahmed et al. 2010; Bošković et al. 2014; Ooga et al. 2016).

Nucleosome organization has been analyzed using micrococcal nuclease sequencing (MNase-seq) (Henikoff et al. 2011; Kent et al. 2011). As MNase cleaves the linker DNA and produces DNA fragments protected by nucleosomes, deep sequencing of the obtained DNA fragments enables analysis of genome-wide nucleosome positioning and occupancy. Recently, MNase-seq optimized for samples with limited cell numbers was applied to one-cell stage mouse embryos, which revealed the nucleosome assembly and remodeling processes immediately after fertilization (Wang et al. 2022a). However, the remodeling of nucleosome organization during early development as well as the underlying molecular mechanisms remain unclear. In this study, we analyzed nucleosome organization in zygotes and two-cell and eight-cell stage mouse embryos and found that zygotes are characterized by globally fuzzy nucleosomes. Furthermore, we found that YY1, expressed upon ZGA, dictates the de novo formation of well-positioned nucleosome arrays at the regulatory elements. Thus, our findings demonstrate the coordination between the embryonic transcriptional program and the remodeling of nucleosome organization during early mouse development.
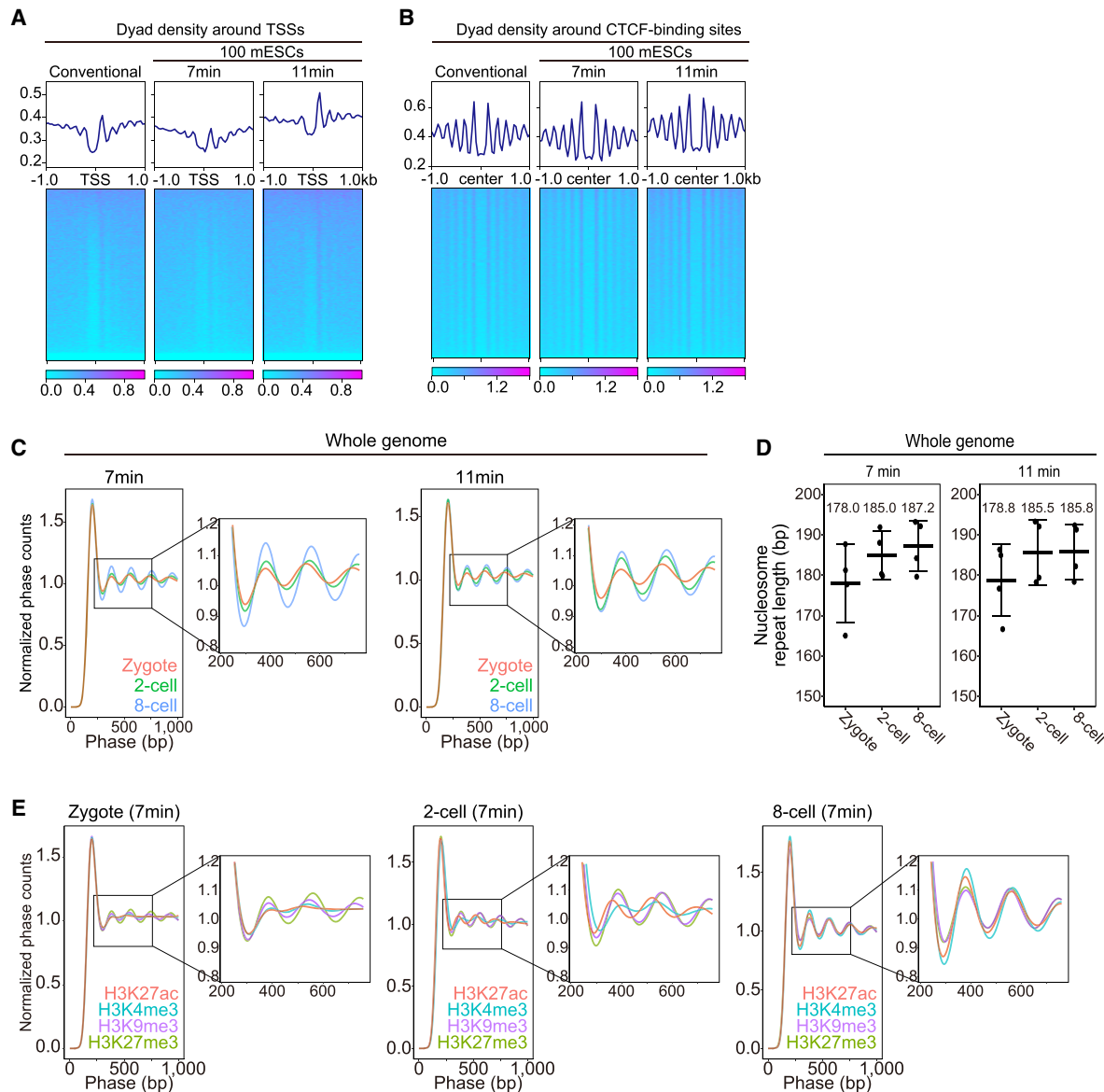
Results

Zygotes possess globally fuzzy nucleosomes

To elucidate the nucleosome dynamics in early mouse embryos, we first established a low-input MNase-seq (liMNase-seq) method using 100 mouse embryonic stem cells (mESCs). We adopted MNase digestion time points, which mainly produce mononucleosomal and dinucleosomal fragments to avoid chromatin underdigestion or overdigestion. Because the degree of MNase digestion affects the MNase-seq results (Henikoff et al. 2011; Mieczkowski et al. 2016), we prepared samples with two different MNase digestion times (7 or 11 min) (Supplemental Fig. S1A). In this study, we drew conclusions that are supported by both sets of data. This MNase titration enabled us to omit gel purification of mononucleosomal DNA fragments, which is considered to be the major cause of loss

of materials in a conventional MNase-seq assay. For nucleosome positioning analyses after sequencing, we used non-redundant mononucleosomal-sized DNA fragments (ranging between 141 and 180 bp) and computed the dyad density. Our liMNase-seq data from 100 mESCs reflected publicly available MNase-seq data (Voong et al. 2016); highly similar patterns of positioned nucleosomes were observed around the TSSs and CTCF-binding sites (nucleosomes whose positions are clearly visible in average plots or heat maps are referred to as [well-]positioned nucleosomes throughout this article) (Fig. 1A,B).

Next, we explored the nucleosome organization in mouse embryos at the late zygotes and late two-cell and eight-cell stages. Biological replicates were prepared for each MNase digestion condition (Supplemental Fig. S1B). After confirming reproducibility (Supplemental Fig. S1C), the replicate data were merged to obtain sufficient read coverage. To characterize the global nucleosome organization for each developmental stage, we performed the phasogram analysis, which generated a histogram of internucleosomal distances at a genome-wide scale (Valouev et al. 2011). In a wave-like pattern of the phasogram, the periodic presence of sharp wave peaks and valleys (i.e., large amplitude) indicates that the spacing between the nucleosomes is consistent and regular. In contrast, a smaller amplitude indicates a large variance in the nucleosome–nucleosome spacing. The amplitude of the phasogram plots became larger along with developmental progression, indicating that nucleosome spacing becomes more uniform during early development (Fig. 1C; Supplemental Fig. S1D). In addition, there was a slight difference in phase; the zygotes showed shorter distances between wave peaks, indicating that the overall nucleosome repeat length is slightly shorter in zygotes (Fig. 1D). These differences are independent of MNase digestion time and therefore are not due to variations in sensitivity to MNase. Thus, these results suggest that the global presence of "fuzzy" nucleosomes characterizes the zygote.

Mouse zygotes are characterized by a noncanonical distribution of histone modifications (Xia and Xie 2020). To investigate whether the observed nucleosome organization in zygotes is linked to the noncanonical epigenetic signatures, we analyzed the nucleosome spacing at H3K4me3-, H3K27ac-, H3K9me3-, and H3K27me3-marked regions (Dahl et al. 2016; Liu et al. 2016; Wang et al. 2018a, 2022b). In all the developmental stages analyzed, lower uniformity in spacing was consistently observed at the euchromatic region marked by H3K4me3 or H3K27ac, whereas relatively high uniformity was observed in the H3K27me3-marked region (Fig. 1E; Supplemental Fig. S1E). However, in zygotes, the phasogram showed much flatter patterns than those in two-cell or eight-cell embryos regardless of the histone marks, and nucleosome spacing in both the euchromatic and heterochromatic regions became more uniform during zygote-to-eight-cell development (Fig. 1E; Supplemental Fig. S1E). These results indicate that a higher degree of variance in nucleosome spacing is prevalent in both the euchromatic and heterochromatic regions in zygotes and cannot be explained by the distribution of these histone marks. There

Figure 1. Dynamic changes in nucleosome spacing during early mouse development. (*A*) Normalized dyad density around TSSs in mESCs. Results from previously published conventional MNase-seq data (Voong et al. 2016) and liMNase-seq data in this study are shown. (*B*) Normalized dyad density around the CTCF-binding sites in mESCs. Results from previously published conventional MNase-seq data (Voong et al. 2016) and liMNase-seq data in this study are shown. (*C*) Phasogram plots showing genome-wide internucleosomal distances in early mouse embryos. Results from two different MNase digestion times are shown in the *left* and *right* panels, respectively. (*D*) Nucleosome repeat length in embryos at the indicated developmental stage. Each dot represents the distance between adjacent peaks in a phasogram. The average distance, which corresponds to the average nucleosome repeat length, is indicated. Error bar indicates SD. (*E*) Phasogram plots showing internucleosomal distances at the genomic regions marked by H3K27ac (red) (Dahl et al. 2016; Wang et al. 2022b), H3K4me3 (blue), H3K27me3 (green) (Liu et al. 2016), and H3K9me3 (purple) (Wang et al. 2018a) in zygotes (*left*) and two-cell (*middle*) and eight-cell (*right*) embryos. Results from liMNase-seq with 7-min MNase digestion are shown.

might be an unknown mechanism that progressively alters nucleosome spacing during early development.

Remodeling of nucleosome organization at promoters during early development

Next, we analyzed the nucleosome positioning around the TSSs. A well-defined pattern of nucleosome positioning,

characterized by the presence of NDRs accompanied by well-positioned nucleosome arrays downstream from the TSSs, was observed in two-cell and eight-cell embryos (Fig. 2A). Nucleosomes corresponding to +1 to +5 were observed at these stages. In contrast, in zygotes, such nucleosome arrays were only partially formed, and only +1 and −1 nucleosomes flanking the NDRs were evident. The formation of NDRs flanked by well-positioned
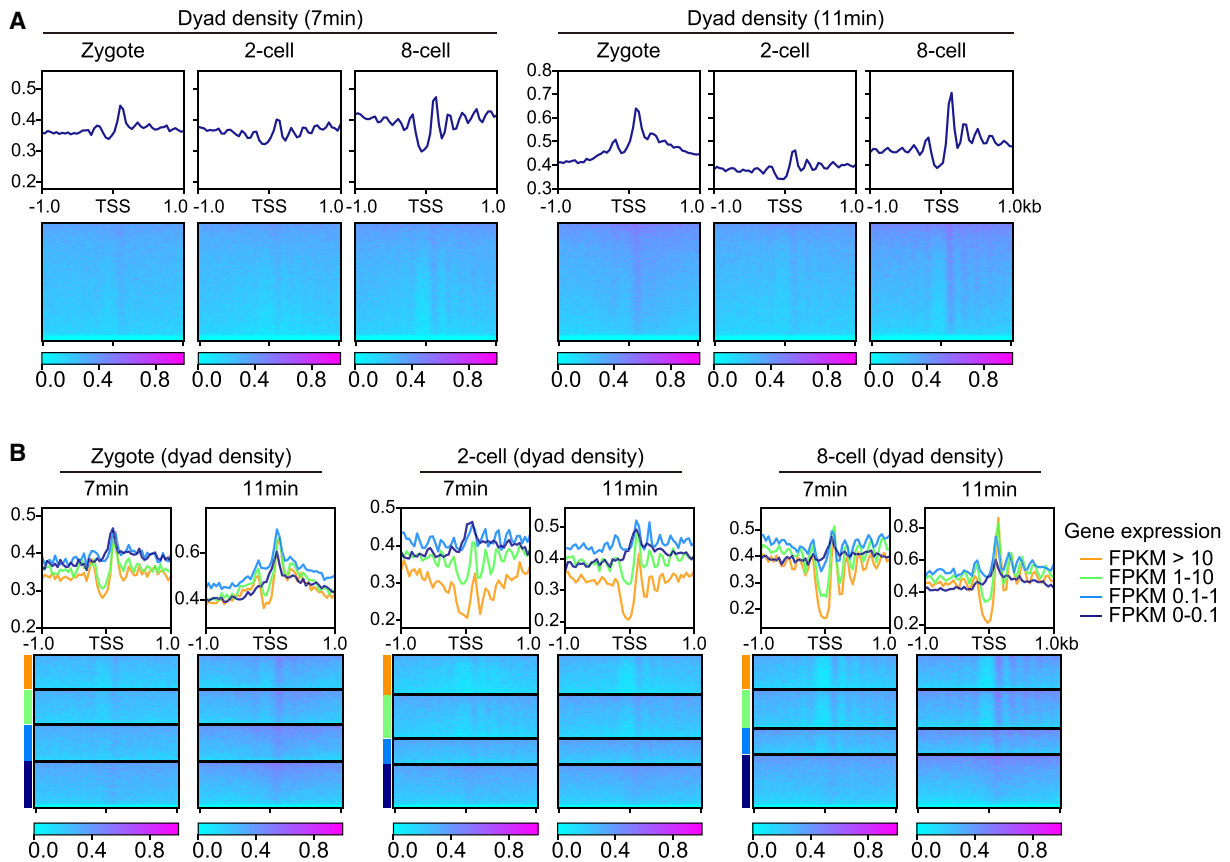
Figure 2. Remodeling of nucleosome organization at promoters during early development. (*A*) Normalized dyad density around the TSSs of all genes in zygotes and two-cell and eight-cell embryos. Results from liMNase-seq with 7-min (*left*) and 11-min (*right*) MNase digestion are shown. (*B*) Normalized dyad density around the TSSs. TSSs were classified by their corresponding gene expression levels in zygotes (*left*) and two-cell (*middle*) and eight-cell (*right*) embryos. Results from two different MNase digestion times are shown.

nucleosome arrays was correlated with gene expression levels in two-cell and eight-cell embryos, whereas such a correlation was not clearly observed in zygotes (Fig. 2B). Transcriptional activity in zygotes is not well represented in RNA-seq data due to carryover of maternal RNA. We then analyzed nucleosome positioning at the gene loci showing promoter RNA polymerase II (Pol II) enrichment (Liu et al. 2020). In contrast to the two-cell and eight-cell embryos, well-positioned nucleosome arrays were still absent at the promoters with Pol II enrichment in zygotes (Supplemental Fig. S2A). The promoters of the major ZGA genes, which undergo transcriptional activation at the two-cell stage, formed well-positioned nucleosome arrays at the two-cell stage (Supplemental Fig. S2B). Therefore, nucleosomes are fuzzily positioned even at the Pol II-associated promoters in zygotes, and well-positioned nucleosome arrays can be established at active promoters after the two-cell stage.

Suppression of CAF-1 activity in mESCs reprograms nucleosome organization

The fact that nucleosome spacing unique to zygotes cannot be explained by representative histone modification patterns led us to hypothesize that the noncanonical histone H3.3 landscape in zygotes, in which histone H3.3 is predominantly distributed across the genome independently of histone modification patterns (Ishiuchi et al. 2021), might be linked to this observation. We previously showed that suppression of the replication-dependent H3.1/H3.2 deposition, mediated by the CAF-1 histone chaperone complex, was sufficient to induce a zygote-like H3.3 distribution in mESCs (Ishiuchi et al. 2021). To address the possible link between these previous findings and global nucleosome fuzziness, we depleted p150, an essential subunit of the CAF-1 complex (Smith and Stillman 1989), in mESCs and performed liMNase-seq. We confirmed that the H3.1/H3.2 level in chromatin decreased upon p150 depletion, whereas the H3.3 level increased to a slight extent (Fig. 3A; Supplemental Fig. S3A). Nucleosome arrays around TSSs or CTCF-binding sites were largely unaffected by p150 depletion (Fig. 3B, C). However, we observed clear changes in the global nucleosome spacing; the phasogram pattern was much more flattened in p150-depleted mESCs compared with that in controls, indicating that the uniformity in internucleosomal spacing was reduced upon p150 depletion (Fig. 3D). These changes in nucleosome organization were
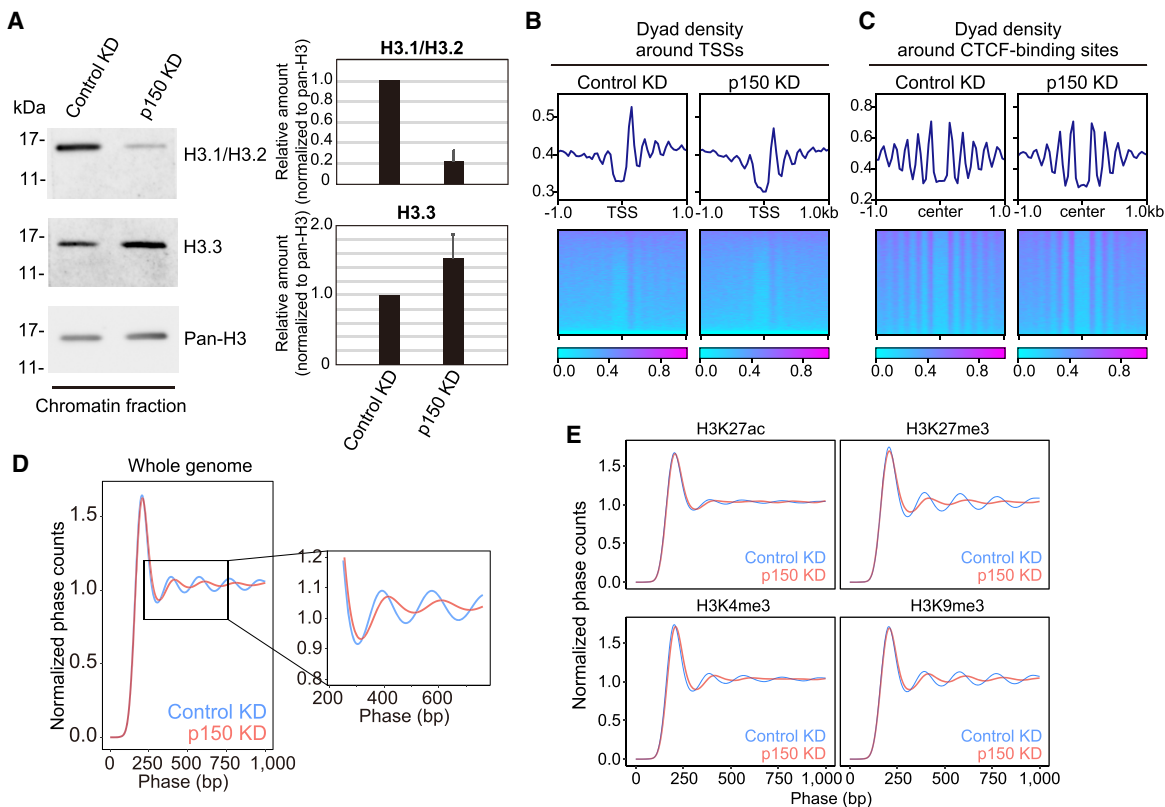
Figure 3. p150 depletion in mESCs reprograms nucleosome organization. (*A*) Western blots showing the changes in the composition of histone H3 variants in chromatin upon p150 depletion. (*Left*) Western blots for H3.1/H3.2, H3.3, and pan-H3 were performed for the chromatin fraction. (*Right*) The data from three independent experiments were quantified and are shown in the bar graph. (*B*) Normalized dyad density around the TSSs in control and p150-depleted mESCs. (*C*) Normalized dyad density around the CTCF-binding sites in control and p150-depleted mESCs. (*D*) Phasogram plots showing genome-wide internucleosomal distances. The region outlined by the square is magnified. Samples analyzed are indicated in different colors. (*E*) Phasogram plots showing the internucleosomal distances at the genomic regions marked by H3K27ac, H3K4me3, H3K9me3, and H3K27me3 in mESCs. ChIP-seq data for H3K27ac (Kurimoto et al. 2015), H3K4me3, H3K9me3, and H3K27me3 (Wang et al. 2018a) were used.

consistently observed in both the euchromatic and heterochromatic regions, as similarly observed in zygotes (Fig. 3D,E). However, the patterns did not match perfectly due to their phase differences (Supplemental Fig. S3B). This indicates that although nucleosome spacing is heterogeneous in both zygotes and p150-depleted mESCs, the overall internucleosomal distances are different between these cells. While p150 depletion was not sufficient to fully mimic nucleosome organization in zygotes, the suppression of CAF-1 activity in mESCs activated the expression of zygotically expressed genes, including Dux (Ishiuchi et al. 2015; Hendrickson et al. 2017; Sugie et al. 2020). Thus, the presence of globally fuzzy nucleosomes may be linked to the initiation of early embryonic transcriptional programs.

Identification of DNA-binding factors mediating nucleosome organization in early mouse embryos

The results above indicate that nucleosome positioning at the TSSs as well as global nucleosome spacing becomes well defined during development. We then speculated

that at least a part of these remodeling processes might be facilitated by DNA-binding factors expressed in early embryos. Well-positioned nucleosome arrays are often associated with NDR formation. Furthermore, NDRs colocalize with DNase I-hypersensitive sites (DHSs) (Wang et al. 2012; Chereji and Clark 2018). Based on these facts, we focused on DNA motifs enriched at DHSs in early embryos (Lu et al. 2016). To establish and validate our strategy to identify factors mediating nucleosome positioning from DNA motifs, we extracted genomic regions containing a consensus CTCF-binding motif and examined DNase I sensitivity and nucleosome positioning around these regions in mESCs. These genomic regions could be divided into two groups, depending on whether NDRs were formed. Those with NDRs, referred to as CTCF footprint (+) regions, showed relatively high DNase-seq signals and well-positioned nucleosome arrays, confirming that the regulatory factors mediating local nucleosome positioning can be identified based on the enriched motifs at the DHSs (Fig. 4A). Considering the fact that nucleosome positioning and spacing are progressively defined during development, we first identified DHSs in developmentally
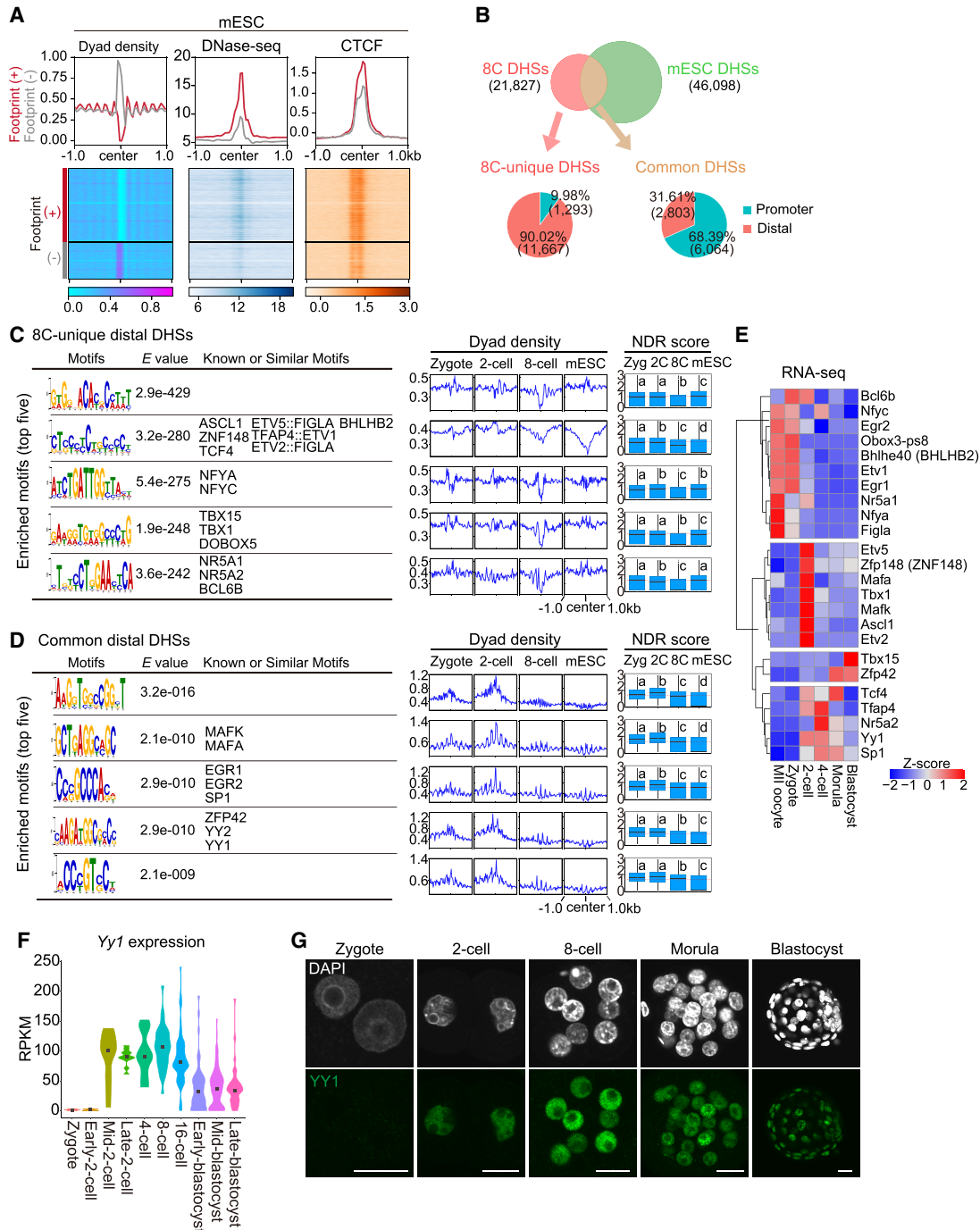
Figure 4. Identification of transcription factors that potentially regulate nucleosome positioning in early mouse embryos. (*A*, *left*) Normalized dyad density around the CTCF consensus sequences (YGCCMYCTNSYGG) in mESCs. These regions are divided into two groups according to the presence of NDRs. Those with NDRs, referred to as footprint (+) regions, are indicated by red plots. DNase-seq signals (*middle*) and CTCF enrichment (*right*) are also shown by average plots and heat maps. (*B*, *top*) Venn diagrams showing the overlap between DHSs in eight-cell embryos and those in mESCs. (*Bottom*) DHSs unique to eight-cell embryos and those common to eight-cell embryos and mESCs are further divided into the promoter-proximal (TSS ± 1 kb) and promoter-distal DHSs. (*C*,*D*) Motif analysis for distal DHSs unique to eight-cell embryos (*C*) and for those common to both eight-cell embryos and mESCs (*D*). (*Left*) Up to five top enriched motifs are shown. Average plots showing normalized dyad density (*middle*) and box plots showing NDR scores [$\log_2$(NDR score + 1)] (*right*) are indicated (a–d indicate significant differences between different characters; $P < 0.05$, Tukey multiple comparison test). (*E*) Heat maps showing expression of the indicated transcription factors. Published RNA-seq data (Abe et al. 2015) were used and are shown as Z-score based on FPKM values. (*F*) Violin plots showing *Yy1* expression levels in early mouse embryos based on scRNA-seq data (Deng et al. 2014). (*G*) Immunostaining for YY1 in early mouse embryos. Representative images from two independent experiments using at least 10 embryos per experiment are shown. Scale bar, 20 μm.

advanced eight-cell embryos as well as in mESCs and focused our analysis on promoter-distal DHSs to exclude the contribution of transcription to nucleosome organization (Fig. 4B). Independent enriched motifs were identified from the distal DHSs unique to eight-cell embryos and those common to both eight-cell embryos and mESCs (Fig. 4C,D). As expected, NDRs were generally formed in regions containing the identified motifs by the eight-cell stage (Fig. 4C,D). These NDRs were typically flanked by positioned nucleosomes but not always, suggesting that NDR formation per se is not sufficient to position the neighboring nucleosomes.

The TFs that can potentially recognize the identified motifs were considered as candidate factors mediating nucleosome positioning (Fig. 4C,D). We noticed that some of them are expressed upon ZGA (Fig. 4E). This finding led us to hypothesize that ZGA-dependent TF expression might trigger the remodeling of nucleosome organization. We then focused on YY1 because *Yy1* was transcribed upon major ZGA at the two-cell stage (Fig. 4F), and well-positioned nucleosome arrays emerged at the YY1 motif-containing regions only after ZGA (Fig. 4D). Similarly, remodeling of nucleosome positioning during development was observed at the YY1-binding sites defined by YY1 ChIP-seq data obtained from mESCs (Supplemental Fig. S4A). We confirmed that YY1 protein is detectable only after the two-cell stage (Fig. 4G). YY1 interacts with chromatin remodeling complexes and functions as a regulator of transcription (Cai et al. 2007; Wang et al. 2018b; Verheul et al. 2020). YY1 has been reported to be a key regulator of enhancer–promoter interactions (Weintraub et al. 2017), but this view appears to require reconsideration (Hsieh et al. 2022). In addition, although YY1 is a ubiquitously expressed protein, YY1 exerts its function in a cellular context-dependent manner (Donohoe et al. 1999; Kleiman et al. 2016; Beagan et al. 2017; Weintraub et al. 2017; Verheul et al. 2020). Despite these previous studies on YY1, the function of YY1 in early mouse embryos as well as in nucleosome remodeling has been poorly characterized.

### YY1 depletion causes a developmental delay at the morula-to-blastocyst transition

To directly test whether the zygotic expression of YY1 is required for the remodeling of nucleosome organization, we introduced siRNA against *Yy1* into zygotes to knock down its expression (Fig. 5A). Two independent siRNAs efficiently suppressed YY1 expression (Fig. 5B,C). *Yy1* knockdown (KD) embryos displayed a clear delay in development at the morula-to-blastocyst transition (Fig. 5D,E). The developmental delay at the morula-to-blastocyst transition was rescued by coinjecting siRNA-resistant *Yy1* mRNA, indicating that the observed phenotype is caused by YY1 depletion (Fig. 5F; Supplemental Fig. S4B, C). Since *Yy1* KD embryos reached the blastocyst stage with some delay, their developmental potential was further examined by embryo transfer. We found that *Yy1* KD strongly reduced the birth rates (Fig. 5G,H). Thus, the presence of YY1 at the early stage of mouse development is important for full-term development, which is

consistent with the previous observation that YY1 is required for embryonic development as well as for the differentiation potential of mESCs (Donohoe et al. 1999; Weintraub et al. 2017).

YY1 regulates nucleosome organization at enhancer-like regions in early embryos

We then collected *Yy1* KD embryos at the eight-cell stage in which developmental delay was not observed and performed liMNase-seq. Nucleosome organization at the TSSs or CTCF-binding sites was largely unaffected by *Yy1* KD (Supplemental Fig. S5A,B), and uniformity in nucleosome spacing was only slightly reduced upon *Yy1* KD (Supplemental Fig. S5C). To investigate the effect of YY1 depletion at the YY1-binding sites, we performed CUT&RUN for YY1 at the eight-cell stage. YY1 CUT&RUN data were highly reproducible (Fig. 6A; Supplemental Fig. S6A), and the YY1-binding motif was found as the most enriched motif in the YY1 CUT&RUN peaks (Fig. 6B). Based on these results, we determined that the CUT&RUN for YY1 was successful. Comparison of YY1-binding sites in eight-cell embryos with those in mESCs and differentiated cells (neuronal precursor cells and B cells) indicated that the highest overlap is found between eight-cell embryos and mESCs, whereas a number of YY1-binding sites were specific to eight-cell embryos (Supplemental Fig. S6B). The eight-cell embryo-specific YY1-binding sites were associated with high chromatin accessibility at the eight-cell stage (Supplemental Fig. S6C). As expected, these YY1-binding sites were flanked by well-positioned nucleosomes at the eight-cell stage (Fig. 6C; Supplemental Fig. S6D). Notably, in zygotes, these YY1-binding sites were occupied by nucleosomes, and well-positioned nucleosome arrays were absent. These results indicate that nucleosome remodeling occurs at these YY1-binding sites concurrently with the expression of YY1 during early development.

To precisely understand the contribution of YY1 to nucleosome remodeling in early mouse embryos, we extracted the YY1-binding sites where NDRs are formed de novo during early development, which we refer to here as YY1 footprint (+) regions (Fig. 6D, green plots). Among the 6667 YY1 footprint (+) regions, 4428 (66.4%) failed to form NDRs flanked by well-positioned nucleosome arrays upon *Yy1* KD at the eight-cell stage; therefore, nucleosome remodeling at these 4428 regions was dependent on YY1 (Fig. 6D, red plots). We noticed that the nucleosome organization at the YY1-dependent regions in *Yy1* KD eight-cell embryos remained similar to that in normal zygotes in which YY1-binding sites were highly occupied by nucleosomes. This appears to be dependent on the underlying DNA sequences, as the dinucleotides CC, GG, and CG, which show greater affinity for nucleosomes (Kaplan et al. 2009; Lai and Pugh 2017), were enriched at these sites (Fig. 6E). To analyze the effect of YY1 depletion on gene expression, we performed RNA-seq for *Yy1* KD eight-cell embryos. We detected a few differentially expressed genes (13 up-regulated and 36 down-regulated genes; false discovery rate <0.05) (Fig. 6F; Supplemental Table S1). Thus, *Yy1* KD on the transcriptome of eight-
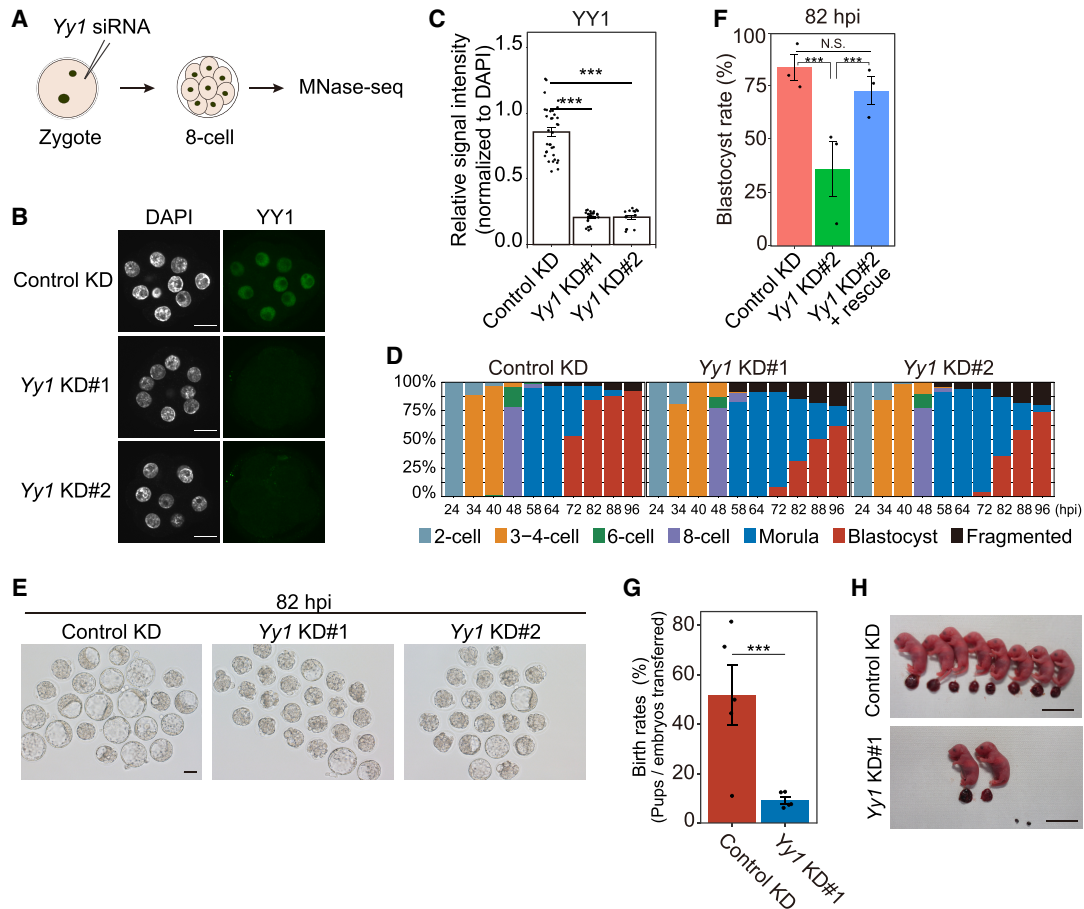
Figure 5. YY1 depletion impairs embryonic development. (*A*) Scheme showing the experiments for *Yy1* knockdown. (*B*) Representative images of immunostaining for YY1 upon *Yy1* KD. Eight-cell embryos were used for immunostaining. Scale bar, 20 μm. (*C*) Plots showing YY1 signal intensity in eight-cell embryos. Each dot represents the nuclear YY1 signal intensity normalized by the signal intensity of DAPI. (***) $P < 0.001$, Wilcoxon rank sum exact test (pairwise comparisons and Bonferroni adjustment). Data shown are mean ± SEM. n = 18 control KD, n = 22 *Yy1* KD#1, and n = 13 *Yy1* KD#2 embryos from three independent experiments. (*D*) Stacked bar charts showing the developmental progression of control and *Yy1* KD embryos. Cultured embryos were observed at the indicated time points (hours post-insemination [hpi]). n = 64 control KD, n = 62 *Yy1* KD#1, and n = 57 *Yy1* KD#2 embryos from three independent experiments. (*E*) Images of control and *Yy1* KD embryos. Embryos were observed at 82 h postinsemination (hpi). Scale bar, 50 μm. (*F*) Bar plots showing the blastocyst rate in the indicated samples. The blastocyst rates at 82 hpi in control, *Yy1* KD, and rescue embryos are shown. n = 59 control KD, n = 61 *Yy1* KD#2, and n = 57 *Yy1* KD#2 + siRNA-resistant *Yy1* mRNA embryos from three independent experiments. Data shown are mean ± SEM. (***) $P < 0.001$, χ^2 test. (*G*,*H*) Effect of *Yy1* KD on full-term development. (*G*) Each dot shows the birth rates following embryo transfer. Data shown are mean ± SEM. (***) $P < 0.001$, χ^2 test. Seventy-five two-cell stage embryos were transferred to pseudopregnant mice for each experimental group. Three independent experiments were performed. (*H*) Representative images of mouse pups derived from control (*top*) and *Yy1* KD (*bottom*) embryos. Scale bar, 2 cm.

cell embryos was minimal, which is highly reminiscent of the limited effect of the depletion of chromatin structural proteins YY1 or CTCF on gene expression in other cell types (Nora et al. 2017; Hyle et al. 2019; Andreu et al. 2022; Hsieh et al. 2022). Taken together, these results indicate that YY1 regulates nucleosome remodeling by the eight-cell stage without having an immediate impact on gene expression.

The YY1-dependent regions included 584 promoter-proximal and 3844 promoter-distal regions. Although both of them showed compromised nucleosome organization in the absence of YY1, the distal regions showed higher nucleosome occupancy (Fig. 6G). To explore the

possible functionality of these YY1-dependent regions as regulatory elements in early embryos, we examined the enrichment of H3K27ac, an active enhancer mark. We found that a large fraction of these regions becomes highly enriched in H3K27ac around the eight-cell and morula stages (Fig. 6G). Notably, the enrichment of H3K27ac was not maintained in mESCs or in epiblast-like cells (EpiLCs), suggesting that the identified YY1-dependent regions function specifically in early embryos (Supplemental Fig. S6E). Collectively, these results indicate that YY1 regulates nucleosome organization at enhancer-like regulatory elements, where H3K27ac levels are dynamically controlled during early mouse development.
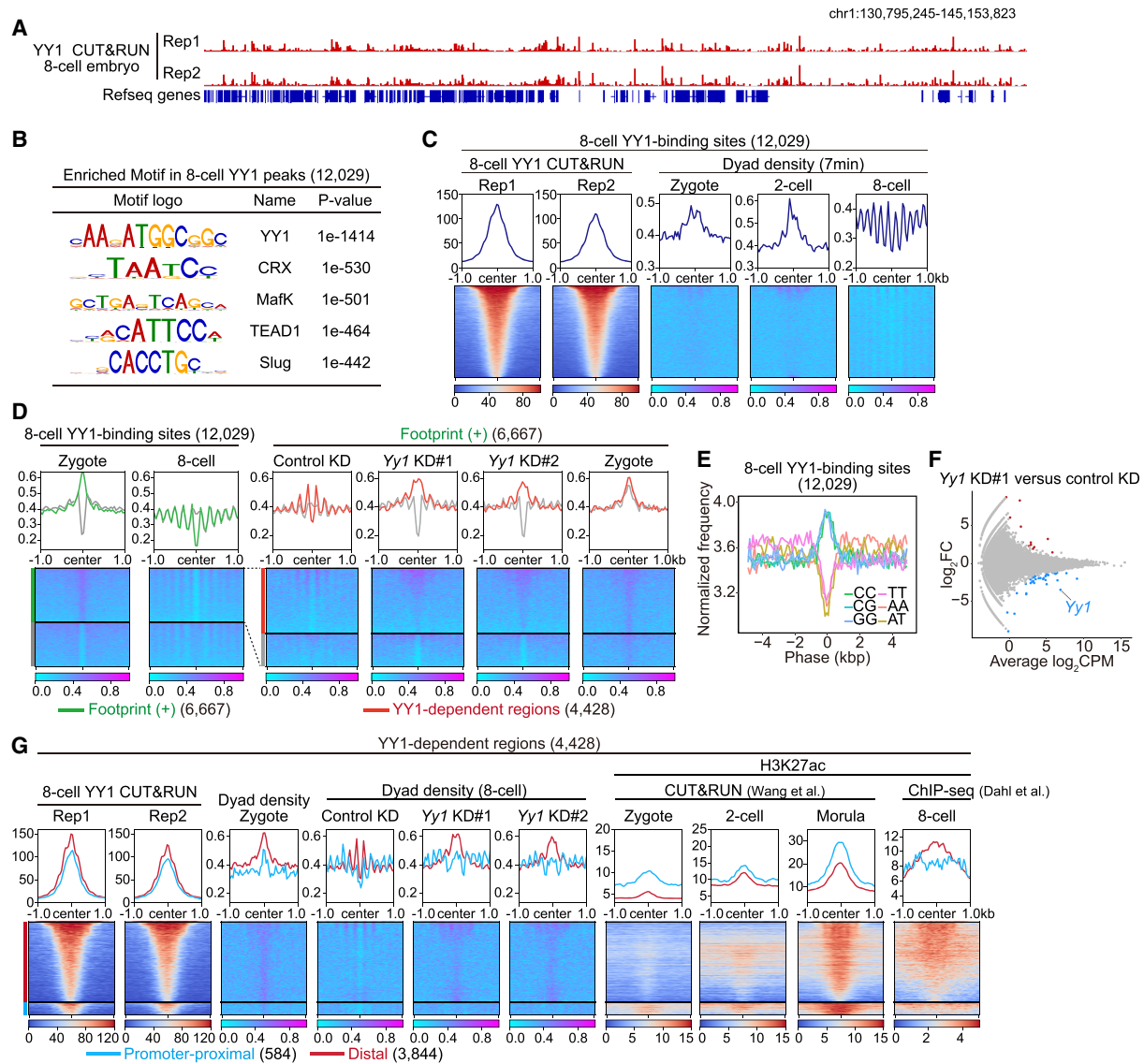
Figure 6. YY1 regulates nucleosome organization at the enhancer-like regions in early mouse embryos. (*A*) Genome browser snapshot showing YY1 CUT&RUN signals in eight-cell embryos. (*B*) Motif analysis of YY1 CUT&RUN peaks in eight-cell embryos. The top five enriched motifs are shown. (*C*) Average plots and heat maps showing the enrichment of YY1 at the YY1-binding regions and the dyad density at the same regions in zygotes and two-cell and eight-cell embryos. (*D*) Normalized dyad density around the YY1-binding sites in zygotes and eight-cell embryos. The YY1-binding sites in zygotes and eight-cell embryos were divided into two groups depending on the de novo formation of NDRs during the zygote-to-eight-cell transition. Those showing the de novo formation of NDRs are referred to as footprint (+) regions (green plots). These footprint (+) regions were further classified into two groups according to their dependency on YY1 to create NDRs in eight-cell embryos. YY1-dependent regions are shown by red plots. (*E*) Plots showing the normalized frequency of the indicated dinucleotides around the YY1-binding sites. The center of the *X*-axis (0 kb) corresponds to the center of YY1-binding sites. (*F*) MA plots showing the changes in gene expression between control and *Yy1* KD eight-cell embryos. Differentially expressed genes were defined by FDR <0.05. Up-regulated (*n* = 13) and down-regulated (*n* = 36) genes in *Yy1* KD embryos are colored in red and blue, respectively. (*G*) Average plots and heat maps showing YY1 enrichment, dyad density, and H3K27ac enrichment around the YY1-dependent regions in the indicated samples. These regions were divided into promoter-proximal (blue, TSS ± 1 kb) and promoter-distal (red) regions. For H3K27ac enrichment, CUT&RUN data for zygotes and two-cell and morula embryos (Wang et al. 2022b) and ChIP-seq data for eight-cell embryos (Dahl et al. 2016) were used.

Discussion

In this study, we delineated the remodeling of nucleosome organization during early mouse development and identified nucleosome organization unique to zygotes, characterized by globally heterogeneous nucleosome–nucleosome spacing. Given that nucleosomes are inhibitory to transcription, the global presence of obscurely positioned nucleosomes may allow promiscuous transcription from the genome (Abe et al. 2015). We consider the

following possibilities on this observation: (1) Zygotes possess relatively unstable or mobile (i.e., fuzzy) nucleosomes across the genome, or (2) nucleosomes are stable, but their spacing is highly variable. The former possibility might be supported by previous findings that zygotes show relatively high histone mobility (Ooga et al. 2016). We found that the suppression of CAF-1 activity in mESCs was sufficient to induce heterogenous nucleosome spacing. However, the suppression of CAF-1 activity in mESCs was not sufficient to fully recapitulate the nucleosome organization observed in zygotes. CAF-1 KD increased nucleosome spacing and linker DNA length possibly due to acutely reduced nucleosome density. On the other hand, zygotes showed rather shorter nucleosome spacing than other cells while showing high heterogeneity. This may suggest the presence of an unknown mechanism that facilitates nucleosome fuzziness independently of the nucleosome density in zygotes. Thus, the molecular basis underlying heterogenous nucleosome spacing in zygotes is still unclear, and further investigations are needed.

Our study revealed the essential roles of YY1 in the remodeling of nucleosome organization during early mouse development. YY1 depletion allows embryonic development to the blastocyst stage (Donohoe et al. 1999); however, our study clearly indicates that defects in nucleosome organization are already detectable at an earlier developmental stage. We speculate that nucleosome remodeling mediated by YY1 might play a primary role in moving and positioning nucleosomes and creating a chromatin environment required for development. In this context, it would be intriguing to examine whether YY1 activity meets the criteria for a pioneer transcription factor (Zaret and Mango 2016). In the absence of YY1, nucleosomes were preferentially located on the YY1-binding sites, presumably in a DNA sequence-dependent manner. The presence of sequences preferred by nucleosomes at regulatory elements may be advantageous for robustly limiting chromatin accessibility until they are recognized by DNA-binding factors at a desired time. YY1-binding sites acquired the active enhancer mark H3K27ac around the eight-cell and morula stages. However, *Yy1* KD minimally affected the transcriptome of eight-cell embryos, similar to what was observed in mESCs in a recent study (Hsieh et al. 2022). In addition, the acute depletion of YY1 minimally affected enhancer–promoter interaction in mESCs (Hsieh et al. 2022). Considering these observations, we prefer a model in which YY1 and its binding partners primarily act to create an organized local chromatin environment at enhancers and/or promoters whose activities are subsequently cooperatively controlled by other TFs (Supplemental Fig. S6F). This is supported by our finding that YY1-binding sites are also enriched in DNA motifs recognized by TFs other than YY1. In this scenario, the YY1-bound enhancer-like regions in eight-cell embryos may not be fully active or functional yet at this developmental stage, which could explain why the transcriptome was affected only mildly by *Yy1* KD. Through its nucleosome remodeling activity, zygotically expressed YY1 may sustain embryonic developmental potency through its possible bookmarking activity (Hsieh et al. 2022).

Materials and methods

Animals and collection of mouse embryos

All animal experiments were approved by the Animal Experiments Committee of Kyushu University (A20-104) and University of Yamanashi (A4-1) and performed according to the guidelines for animal experiments at Kyushu University and University of Yamanashi. Mice were housed in cages under specific pathogen-free conditions and had free access to water and food. C57BL/6J or BDF1 (C57BL/6N × DBA/2) female mice (8–12 wk old) were superovulated by injecting 5 IU of pregnant mature serum gonadotropin (PMSG), followed by injection of 5 IU of human chorionic gonadotropin (hCG) 46–48 h later. For MNase-seq, the superovulated C57BL/6J female mice were mated with DBA/2 male mice. The zygotes were recovered from the oviducts of female mice at 20 h post-hCG injection (hphCG) and cultured in KSOM medium (Millipore). Embryo samples were collected at defined time periods after hCG injection: 27–28 h for zygotes, 46–48 h for late two-cell stage, or 68–70 h for eight-cell stage. The zona pellucida of embryos was removed by acidic Tyrode's solution (Sigma-Aldrich), and the polar bodies of zygotes were removed by attaching the polar bodies to Petri dishes. The embryos were then washed with M2 medium several times and added to low-bind tubes (Thermo Fisher) containing nucleus EZ lysis buffer (Sigma-Aldrich). Ten microliters of the lysis buffer was used per 100 cells. The lysed embryos were snap-frozen in liquid nitrogen and kept at −80°C.

In vitro fertilization, siRNA injection, and embryo transfer

For in vitro fertilization, spermatozoa were obtained from BDF1 male mice. For capacitation, the spermatozoa were cultured in human tubal fluid (HTF) medium for 1 h before insemination. Cumulus–oocyte complexes were obtained from superovulated BDF1 female mice and inseminated with capacitated sperm in HTF medium. At 1–2 h postinsemination (hpi), the zygotes were washed and cultured in EmbryoMax KSOM medium (Merck Millipore). For Yy1 knockdown, two different silencer select siRNAs (10 μM in H_2O; Thermo Fisher) were injected into the cytoplasm of zygotes at 2–3 hpi. Pronuclear formation was verified at 6 hpi. Two-cell stage embryos were transferred to the oviducts of pseudopregnant ICR female mice. The pups were delivered by caesarian section 18 d postcoitum. For a rescue experiment, Yy1 cDNA carrying five nucleotide substitutions (silent mutations) that conferred resistance against Yy1 siRNA #2 was cloned into pcDNA3.1-polyA83 plasmid, and Yy1 mRNA was prepared by in vitro transcription. This Yy1 mRNA (10 ng/μL) was coinjected with Yy1 siRNA #2.

Immunofluorescence

Zygote, two-cell, eight-cell, morula, and blastocyst stage embryos were collected at 10, 30, 48, 72, and 96 hpi, respectively. Embryos were fixed by 4% paraformaldehyde (PFA) in PBS for 10 min at room temperature and then permeabilized using 0.2% Triton X-100 (Tx) in PBS for 10 min at room temperature. The fixed embryos were washed three times with PBS containing 0.02% Tx and incubated in blocking buffer (3% BSA in PBS) overnight at 4°C. To compare the signal intensity between samples from different developmental stages, the fixed embryos at different stages were pooled in the blocking buffer, and the pooled embryos were treated as a single sample. Embryos were incubated with YY1 antibody (1:500; Santa Cruz Biotechnology sc-7341) overnight at 4°C. Embryos were then washed three times with PBS containing 0.02% Tx and incubated with secondary antibodies against

mouse IgG labeled with Alexa fluor 488 (1:500; Thermo Fisher A-11001) for 1 h at room temperature. The embryos were then mounted on VectaShield (Vector Laboratories) containing DAPI (4′,6-diamidino-2-phenilindole). Fluorescence signals were detected using a confocal microscope (Olympus FV1200). For quantitative analysis, fluorescence signal intensity was measured using Fiji software (Schindelin et al. 2012). YY1 signal in each nucleus was normalized by DAPI signal. Statistical analysis was performed using R (version 4.0.3).

Cell culture

Male mouse embryonic stem cells (B6;129 F1 or JM8A3N1 ES cells) were cultured with the medium that consisted of GMEM (Sigma-Aldrich) containing 15% FBS, 0.1 mM 2-mercaptoethanol, nonessential amino acid, sodium pyruvate, penicillin/streptomycin, LIF, 0.5 µM PD0325901, and 3 µM CHIR99021 on gelatin-coated plates. Lipofectamine RNAi MAX (Thermo Fisher) was used to transfect siRNA into JM8A3N1 ES cells. The effect of RNAi was examined 2 d after transfection. We used Silencer negative control #1 siRNA (Thermo Fisher) as a negative control for siRNA and Silencer select siRNA against Chaf1a (p150) as described before (Ishiuchi et al. 2021).

Chromatin extraction and Western blotting

Bulk chromatin extraction from mESCs was carried out using a published protocol with minor modifications (Méndez and Stillman 2000). Briefly, pelleted cells (7×10^5 cells/replicate) were resuspended in 200 µL of buffer A (10 mM HEPES at pH 7.9, 10 mM KCl, 1.5 mM MgCl$_2$, 0.34 M sucrose, 10% glycerol, 0.1% Triton X-100, complete EDTA-free protease inhibitor cocktail [Sigma Aldrich]) for 10 min at 4°C. After centrifugation at 1300g for 5 min, the supernatant was discarded. The pellet was subjected to one additional wash with buffer A without Triton X-100. The pellet was then resuspended in 100 µL of buffer B (3 mM EDTA, 0.2 mM EGTA, complete EDTA-free protease inhibitor cocktail) and incubated for 30 min at 4°C. After that, samples were once again centrifuged at 1700g for 5 min at 4°C. Finally, chromatin pellets were washed again with buffer B and then resuspended in Laemmli sample buffer. The samples were boiled for 5 min and loaded for SDS-PAGE. Antibodies used for Western blotting were anti-H3.1/H3.2 (1:1000; Active Motif 61629), anti-H3.3 (1:1000; Active Motif 91191), and anti-pan H3 (1:1000; Active Motif 39763). To confirm knockdown efficiency, anti-p150 (1:1000; Proteintech 17037-1-AP) and anti-β-actin (1:10,000; Santa Cruz Biotechnology sc-69879) antibodies were used.

Low-input MNase-seq

The frozen cell or embryo samples were quickly thawed and put on ice. After the addition of 1 µL of 1% Triton X-100/1% deoxycholate solution, MNase digestion was performed by adding 40 µL of MNase master mix as described in the protocol for ULI-NChIP-seq (Brind'Amour et al. 2015). For the titration of MNase activity, MNase digestion was performed for 100 mESCs with different times at 21°C. Seven-minute or 11-min digestion time was applied for all embryo samples except for siRNA-introduced cell samples, which were treated with MNase for 7 min only. After the MNase digestion, MNase activity was stopped by adding 5.5 µL of 100 mM EDTA, and then 4 µL of 1% Triton X-100/1% deoxycholate solution was added. After incubation for 15 min on ice, the samples were mildly vortexed for 30 sec, and 60 µL of SDS-ProK buffer (10 mM Tris-HCl at pH 8.0, 300 mM NaCl, 5 mM EDTA, 1% SDS, 0.5 mg/mL proteinase K)

was added. The samples were incubated for 1 h at 55°C and then subjected to phenol/chloroform extraction. After taking the upper (aqueous) phase, 35 µL of 10 mM Tris-HCl (pH 8.0) was added to the remaining lower phase and then vortexed and centrifuged again to maximize DNA recovery. The resulting upper phase was recovered and combined with the upper phase initially recovered. DNA was precipitated by adding 15 µL of 3 M sodium acetate, 1 µL of Ethachinmate (Nippongene), and 412.5 µL of ethanol. The samples were incubated overnight at −30°C. The samples were centrifuged at 15,000 rpm for >1 h, and the pellets were washed with 70% ethanol. After carefully removing the ethanol, DNA was dissolved in 20 µL of pure water. The DNA was used for library preparation using NEBnext Ultra II DNA library preparation kit (NEB) following the manufacturer's instruction except that all steps were scaled down to be performed with 40% volume and the samples were subjected to PCR amplification for 13 cycles by KAPA HiFi Hot Start DNA polymerase (Kapa Biosystems) using unique dual-index primers (NEB). DNA was purified by adding 0.8× volume of Ampure XP and eluted in 22 µL of 10 mM Tris-HCl (pH 8.0). One microliter of the samples was used for Bioanayzer (Agilent technologies). Paired-end sequencing was performed on a NovaSeq 6000 (53bpX2).

RNA-seq

Eight-cell embryos were collected at 48 hpi, washed three times with PBS containing 0.1% BSA, flash-frozen with liquid nitrogen, and stored at −80°C until use. Each replicate contained 10 eight-cell embryos. SMART-seq stranded kit (Takara) was used to prepare RNA-seq libraries. The first and second amplification steps were carried out for 10 and 13 cycles, respectively. Paired-end sequencing was performed using an Illumina NovaSeq 6000 (53bpX2).

MNase-seq data processing

Trimming and mapping MNase-seq paired-end reads were aligned to the mouse genome (mm10) using Bowtie2 (version 2.4.3) (Langmead and Salzberg 2012) with options "--no-mixed --no-discordant –no-unal" after removing adaptor sequences and low-quality reads by Trim Galore! (version 0.6.7, Babraham Institute). Reads from PCR duplicates were removed by using SAMtools (version 1.4.1) (Li et al. 2009) "markdup" with an option "-r." We then extracted mononucleosomal DNA fragments (141–180 nt) for further analyses. After confirming reproducibility between replicates, they were merged. To exclude the possibility that differences in the number of reads used for the analysis affected the results, we adjusted the read numbers of each sample for all the analyses.

Nucleosome positioning and occupancy To analyze the nucleosome dyad frequency, BAM files extracted from mononucleosomal DNA fragments were converted into BED format files for calling the midpoint of fragments. The BED files were again converted to BAM format using BEDTools (version 2.30.0) (Quinlan and Hall 2010) "bedtobam" and converted to bigWig files by using bamCoverage function in deepTools (version 3.5.1) (Ramírez et al. 2016) with options "--binSize 1 --normalizeUsing RPKM." Genomic annotation files were downloaded from UCSC table browser. Plots for dyad frequency at defined genomic regions were generated by computeMatrix and plotHeatmap functions in deepTools. Phasograms were depicted by using Numap (Valouev et al. 2011). The data were normalized to total counts and smoothened using "supsmu" function of R. MNase-seq data for mESCs were obtained from GSE82127 (Voong et al. 2016)

and analyzed as described above. For analysis for histone modification marks, we calculated read counts in a 100-kb bin for zygotes and mESCs and a 10-kb bin for two-cell, eight-cell, and morula embryos and then extracted the top 1000 genomic regions (for zygotes and mESCs) or 10,000 genomic regions (for two-cell, eight-cell, and morula stages) enriched in H3K4me3, H3K27ac, H3K9me3, or H3K27me3. To analyze nucleosome-depleted region (NDR) score, the output data from computeMatrix were used. We calculated average dyad density from −60 to +60 bp as well as that from −1 kb to +1 kb and then their ratio. This ratio was also used to detect footprint (+) or (−) regions with an appropriate threshold (>1.5 for nucleosome-occupied regions, and <0.25 for nucleosome-depleted CTCF-binding sites). The YY1 binding sites showing <0.67× changes in NDR scores between zygotes and eight-cell embryos or between control and Yy1 KD embryos were extracted to define footprint (+) regions and YY1-dependent regions, respectively.

Comparison of liMNase-seq data with other data sets Low-input DNase-seq (liDNase-seq) data were obtained from GSE76642 (Lu et al. 2016). ChIP-seq data were obtained from GSE97778, GSE73952, GSE72784, GSE60204, GSE99521, GSE73534, and GSE25197 (Mendenhall et al. 2010; Kurimoto et al. 2015; Dahl et al. 2016; Kleiman et al. 2016; Liu et al. 2016; Weintraub et al. 2017; Wang et al. 2018a). CTCF ChIP-seq data were downloaded from the ENCODE portal (https://www.encodeproject.org) with the following identifiers: ENCFF508CKL, ENCFF683TKC, and ENCFF061WVR. CUT&RUN data were obtained from GSE207222 (Wang et al. 2022b). RNA Pol II data were obtained from GSE135457 (Liu et al. 2020). Reads were aligned to the mouse genome (mm10) using Bowtie2 with a default setting after removing adaptor sequences and low-quality reads by Trim Galore!. Reads from PCR duplicates were removed by using SAMtools "markdup" with an option "-r." BigWig files were generated by using bamCoverage function in deepTools with options "–binSize 10 –normalizeUsing RPKM" or bamCompare function with options "–binSize 10 –normalizeUsing RPKM" for calculation between ChIP and input ratio. To identify DHSs, peak calling was performed with MACS2 (version 2.2.7.1) (Zhang et al. 2008) with options "–mfold 3 500." To identify YY1-binding sites, peak calling was performed with MACS2 with options "-q 0.05 –keep-dup auto." These peak regions were annotated with nearby genes using annotatePeaks.pl (Gencode vM12 database was used) from HOMER (Heinz et al. 2010), and peaks more than ± 1.0 kb away from the TSSs were defined as distal peaks.

CUT&RUN

CUT&RUN was performed as described previously (Ishiuchi et al. 2021) with small modifications. Eight-cell embryos were collected at 50 hpi. Approximately 1500 cells (180 and 220 eight-cell embryos for each replicate sample, respectively) were used per sample, and 2 mM EGTA was included in place of EDTA in the antibody buffer. Incubation with rabbit YY1 antibody (1:100 dilution; Proteintech 22156-1-AP) was performed for 1.5 h at room temperature. After washing with the antibody buffer, the samples were incubated in a wash buffer containing 500 ng/mL protein A–protein G–MNase for 1 h at 4°C. Sequencing libraries were prepared by NEBNext Ultra II DNA library preparation kit (NEB) with 15 cycles of PCR by KAPA library amplification kit (Roche). Long DNA fragments in the libraries were removed by 0.7× AMPure XP (Beckman Coulter). Single-end sequencing was performed on a NextSeq2000 (75bp). CUT&RUN reads were aligned to the mouse genome (mm10) using Bowtie2 (version 2.4.1) (Langmead and Salzberg 2012) after removing adaptor sequences and low-quality reads by Trim Galore! (version 0.6.7; Babraham Institute). Duplicate and low mapping quality reads were removed, and genome coverage tracks were generated by bamCoverage from deepTools (version 3.5.1) (Ramirez et al. 2016) with parameters "--normalizeUsing RPKM --binSize 10." MACS2 (version 2.2.7.1) (Zhang et al. 2008) was used to call peaks with options "-q 0.05 --keep-dup auto." Because CUT&RUN uses MNase, YY1 CUT&RUN peaks were centered at either YY1-bound regions or adjacent nucleosomes. To adjust the phase of nucleosome positioning with respect to YY1-binding sites, the coordinates of YY1 peaks centered at adjacent nucleosomes were shifted by 93 bp (the half-length of the nucleosome repeat length in eight-cell embryos).

Motif analysis

To analyze transcription factor motifs in eight-cell unique DHSs and eight-cell mESC common DHSs, we used MEME-ChIP (version 5.4.1) (Machanick and Bailey 2011) with the following parameters: classic mode/mouse (*Mus musculus*) DNA/HOCOMOCO mouse (v11 core)/second-order model of sequences/minimum width: 6/maximum width: 15/zero or one occurrence per sequence/number of motifs: 5. "findMotifsGenome.pl" from HOMER (v4.11) (Heinz et al. 2010) was used to identify consensus motifs at the YY1-binding sites in eight-cell embryos with the default option.

Calculation of dinucleotide frequency

To calculate dinucleotide frequency, the sequence data were obtained from YY1-binding sites in mESCs using the BEDTools "getfasta" function. The frequency was calculated by counting the number of occurrences of specific dinucleotides and dividing by the number of total dinucleotides. Data were normalized using the "scale" function in R.

RNA-seq data processing

For samples prepared using a SMART-seq stranded kit (Takara), the first three bases of read 2 derived from the SMART-seq stranded adaptor were removed using Trim Galore! before mapping with Hisat2 (version 2.2.1) (Kim et al. 2015). Reads corresponding to ribosomal RNA were removed using the BEDTools "intersectBed" function. Read counts were calculated by featureCounts (Rsubread version 2.4.3 package in R) (Liao et al. 2014), and the expression of each gene annotated by Gencode vM12 was quantified by calculating FPKM (fragments per kilobase of exon per million reads mapped). The resulting read count data were processed using EdgeR (Robinson et al. 2010) to identify differentially expressed genes. A false discovery rate of <0.05, was used to extract differentially expressed genes.

Quantification and statistical analysis

Statistical analyses were implemented with Prism 6 (GraphPad), R (http://www.r-project.org), or Excel (Microsoft) software.

Data availability

All sequencing data have been deposited in the Gene Expression Omnibus (GEO) under the accession number GSE220074.

Competing interest statement

Acknowledgments

References

Abe K, Yamamoto R, Franke V, Cao M, Suzuki Y, Suzuki MG, Vlahovicek K, Svoboda P, Schultz RM, Aoki F. 2015. The first murine zygotic transcription is promiscuous and uncoupled from splicing and 3′ processing. *EMBO J* **34:** 1523–1537. doi:10.15252/embj.201490648

Ahmed K, Dehghani H, Rugg-Gunn P, Fussner E, Rossant J, Bazett-Jones DP. 2010. Global chromatin architecture reflects pluripotency and lineage commitment in the early mouse embryo. *PLoS One* **5:** e10531. doi:10.1371/journal.pone.0010531

Andreu MJ, Alvarez-Franco A, Portela M, Gimenez-Llorente D, Cuadrado A, Badia-Careaga C, Tiana M, Losada A, Manzanares M. 2022. Establishment of 3D chromatin structure after fertilization and the metabolic switch at the morula-to-blastocyst transition require CTCF. *Cell Rep* **41:** 111501. doi:10.1016/j.celrep.2022.111501

Beagan JA, Duong MT, Titus KR, Zhou L, Cao Z, Ma J, Lachanski CV, Gillis DR, Phillips-Cremins JE. 2017. YY1 and CTCF orchestrate a 3D chromatin looping switch during early neural lineage commitment. *Genome Res* **27:** 1139–1152. doi:10.1101/gr.215160.116

Bošković A, Eid A, Pontabry J, Ishiuchi T, Spiegelhalter C, Raghu Ram EV, Meshorer E, Torres-Padilla ME. 2014. Higher chromatin mobility supports totipotency and precedes pluripotency in vivo. *Genes Dev* **28:** 1042–1047. doi:10.1101/gad.238881.114

Brind'Amour J, Liu S, Hudson M, Chen C, Karimi MM, Lorincz MC. 2015. An ultra-low-input native ChIP-seq protocol for genome-wide profiling of rare cell populations. *Nat Commun* **6:** 6033. doi:10.1038/ncomms7033

Cai Y, Jin J, Yao T, Gottschalk AJ, Swanson SK, Wu S, Shi Y, Washburn MP, Florens L, Conaway RC, et al. 2007. YY1 functions with INO80 to activate transcription. *Nat Struct Mol Biol* **14:** 872–874. doi:10.1038/nsmb1276

Chereji RV, Clark DJ. 2018. Major determinants of nucleosome positioning. *Biophys J* **114:** 2279–2289. doi:10.1016/j.bpj.2018.03.015

Dahl JA, Jung I, Aanes H, Greggains GD, Manaf A, Lerdrup M, Li G, Kuan S, Li B, Lee AY, et al. 2016. Broad histone H3K4me3 domains in mouse oocytes modulate maternal-to-zygotic transition. *Nature* **537:** 548–552. doi:10.1038/nature19360

Deng Q, Ramsköld D, Reinius B, Sandberg R. 2014. Single-cell RNA-seq reveals dynamic, random monoallelic gene expression in mammalian cells. *Science* **343:** 193–196. doi:10.1126/science.1245316

Donohoe ME, Zhang X, McGinnis L, Biggers J, Li E, Shi Y. 1999. Targeted disruption of mouse Yin Yang 1 transcription factor results in peri-implantation lethality. *Mol Cell Biol* **19:** 7237–7244. doi:10.1128/MCB.19.10.7237

Eckersley-Maslin MA, Alda-Catalinas C, Reik W. 2018. Dynamics of the epigenetic landscape during the maternal-to-zygotic transition. *Nat Rev Mol Cell Biol* **19:** 436–450. doi:10.1038/s41580-018-0008-z

Fu X, Zhang C, Zhang Y. 2020. Epigenetic regulation of mouse preimplantation embryo development. *Curr Opin Genet Dev* **64:** 13–20. doi:10.1016/j.gde.2020.05.015

Heinz S, Benner C, Spann N, Bertolino E, Lin YC, Laslo P, Cheng JX, Murre C, Singh H, Glass CK. 2010. Simple combinations of lineage-determining transcription factors prime cis-regulatory elements required for macrophage and B cell identities. *Mol Cell* **38:** 576–589. doi:10.1016/j.molcel.2010.05.004

Hendrickson PG, Doráis JA, Grow EJ, Whiddon JL, Lim JW, Wike CL, Weaver BD, Pflueger C, Emery BR, Wilcox AL, et al. 2017. Conserved roles of mouse DUX and human DUX4 in activating cleavage-stage genes and MERVL/HERVL retrotransposons. *Nat Genet* **49:** 925–934. doi:10.1038/ng.3844

Henikoff JG, Belsky JA, Krassovsky K, MacAlpine DM, Henikoff S. 2011. Epigenome characterization at single base-pair resolution. *Proc Natl Acad Sci USA* **108:** 18318–18323. doi:10.1073/pnas.1110731108

Hsieh TS, Cattoglio C, Slobodyanyuk E, Hansen AS, Darzacq X, Tjian R. 2022. Enhancer–promoter interactions and transcription are largely maintained upon acute loss of CTCF, cohesin, WAPL or YY1. *Nat Genet* **54:** 1919–1932. doi:10.1038/s41588-022-01223-8

Hyle J, Zhang Y, Wright S, Xu B, Shao Y, Easton J, Tian L, Feng R, Xu P, Li C. 2019. Acute depletion of CTCF directly affects MYC regulation through loss of enhancer–promoter looping. *Nucleic Acids Res* **47:** 6699–6713. doi:10.1093/nar/gkz462

Isbel L, Grand RS, Schübeler D. 2022. Generating specificity in genome regulation through transcription factor sensitivity to chromatin. *Nat Rev Genet* **23;** 728–740. doi:10.1038/s41576-022-00512-6

Ishiuchi T, Enriquez-Gasca R, Mizutani E, Bošković A, Ziegler-Birling C, Rodriguez-Terrones D, Wakayama T, Vaquerizas JM, Torres-Padilla ME. 2015. Early embryonic-like cells are induced by downregulating replication-dependent chromatin assembly. *Nat Struct Mol Biol* **22:** 662–671. doi:10.1038/nsmb.3066

Ishiuchi T, Abe S, Inoue K, Yeung WKA, Miki Y, Ogura A, Sasaki H. 2021. Reprogramming of the histone H3.3 landscape in the early mouse embryo. *Nat Struct Mol Biol* **28:** 38–49. doi:10.1038/s41594-020-00521-1

Kaplan N, Moore IK, Fondufe-Mittendorf Y, Gossett AJ, Tillo D, Field Y, LeProust EM, Hughes TR, Lieb JD, Widom J, et al. 2009. The DNA-encoded nucleosome organization of a eukaryotic genome. *Nature* **458:** 362–366. doi:10.1038/nature07667

Kent NA, Adams S, Moorhouse A, Paszkiewicz K. 2011. Chromatin particle spectrum analysis: a method for comparative chromatin structure analysis using paired-end mode next-generation DNA sequencing. *Nucleic Acids Res* **39:** e26. doi:10.1093/nar/gkq1183

Kim D, Langmead B, Salzberg SL. 2015. HISAT: a fast spliced aligner with low memory requirements. *Nat Methods* **12:** 357–360. doi:10.1038/nmeth.3317

Kleiman E, Jia H, Loguercio S, Su AI, Feeney AJ. 2016. YY1 plays an essential role at all stages of B-cell differentiation. *Proc Natl Acad Sci USA* **113:** E3911–E3920. doi:10.1073/pnas.1606297113

Kurimoto K, Yabuta Y, Hayashi K, Ohta H, Kiyonari H, Mitani T, Moritoki Y, Kohri K, Kimura H, Yamamoto T, et al. 2015. Quantitative dynamics of chromatin remodeling during germ cell specification from mouse embryonic stem cells. *Cell Stem Cell* **16:** 517–532. doi:10.1016/j.stem.2015.03.002

Lai WKM, Pugh BF. 2017. Understanding nucleosome dynamics and their links to gene expression and DNA replication. *Nat Rev Mol Cell Biol* **18:** 548–562. doi:10.1038/nrm.2017.47

Langmead B, Salzberg SL. 2012. Fast gapped-read alignment with Bowtie 2. *Nat Methods* **9:** 357–359. doi:10.1038/nmeth.1923

Li H, Handsaker B, Wysoker A, Fennell T, Ruan J, Homer N, Marth G, Abecasis G, Durbin R, Genome Project Data Processing S. 2009. The sequence alignment/map format and SAMtools. *Bioinformatics* **25:** 2078–2079. doi:10.1093/bioinformatics/btp352

Liao Y, Smyth GK, Shi W. 2014. Featurecounts: an efficient general purpose program for assigning sequence reads to genomic features. *Bioinformatics* **30:** 923–930. doi:10.1093/bioinformatics/btt656

Liu X, Wang C, Liu W, Li J, Li C, Kou X, Chen J, Zhao Y, Gao H, Wang H, et al. 2016. Distinct features of H3K4me3 and H3K27me3 chromatin domains in pre-implantation embryos. *Nature* **537:** 558–562. doi:10.1038/nature19362

Liu B, Xu Q, Wang Q, Feng S, Lai F, Wang P, Zheng F, Xiang Y, Wu J, Nie J, et al. 2020. The landscape of RNA Pol II binding reveals a stepwise transition during ZGA. *Nature* **587:** 139–144. doi:10.1038/s41586-020-2847-y

Lu F, Liu Y, Inoue A, Suzuki T, Zhao K, Zhang Y. 2016. Establishing chromatin regulatory landscape during mouse preimplantation development. *Cell* **165:** 1375–1388. doi:10.1016/j.cell.2016.05.050

Machanick P, Bailey TL. 2011. MEME-ChIP: motif analysis of large DNA datasets. *Bioinformatics* **27:** 1696–1697. doi:10.1093/bioinformatics/btr189

Mendenhall EM, Koche RP, Truong T, Zhou VW, Issac B, Chi AS, Ku M, Bernstein BE. 2010. GC-rich sequence elements recruit PRC2 in mammalian ES cells. *PLoS Genet* **6:** e1001244. doi:10.1371/journal.pgen.1001244

Méndez J, Stillman B. 2000. Chromatin association of human origin recognition complex, cdc6, and minichromosome maintenance proteins during the cell cycle: assembly of prereplication complexes in late mitosis. *Mol Cell Biol* **20:** 8602–8612. doi:10.1128/MCB.20.22.8602-8612.2000

Mieczkowski J, Cook A, Bowman SK, Mueller B, Alver BH, Kundu S, Deaton AM, Urban JA, Larschan E, Park PJ, et al. 2016. MNase titration reveals differences between nucleosome occupancy and chromatin accessibility. *Nat Commun* **7:** 11485. doi:10.1038/ncomms11485

Nora EP, Goloborodko A, Valton AL, Gibcus JH, Uebersohn A, Abdennur N, Dekker J, Mirny LA, Bruneau BG. 2017. Targeted degradation of CTCF decouples local insulation of chromosome domains from genomic compartmentalization. *Cell* **169:** 930–944.e22. doi:10.1016/j.cell.2017.05.004

Ooga M, Fulka H, Hashimoto S, Suzuki MG, Aoki F. 2016. Analysis of chromatin structure in mouse preimplantation embryos by fluorescent recovery after photobleaching. *Epigenetics* **11:** 85–94. doi:10.1080/15592294.2015.1136774

Quinlan AR, Hall IM. 2010. BEDTools: a flexible suite of utilities for comparing genomic features. *Bioinformatics* **26:** 841–842. doi:10.1093/bioinformatics/btq033

Ramírez F, Ryan DP, Gruning B, Bhardwaj V, Kilpert F, Richter AS, Heyne S, Dündar F, Manke T. 2016. Deeptools2: a next generation web server for deep-sequencing data analysis. *Nucleic Acids Res* **44:** W160–W165. doi:10.1093/nar/gkw257

Robinson MD, McCarthy DJ, Smyth GK. 2010. EdgeR: a Bioconductor package for differential expression analysis of digital gene expression data. *Bioinformatics* **26:** 139–140. doi:10.1093/bioinformatics/btp616

Sadeh R, Allis CD. 2011. Genome-wide 're'-modeling of nucleosome positions. *Cell* **147:** 263–266. doi:10.1016/j.cell.2011.09.042

Schindelin J, Arganda-Carreras I, Frise E, Kaynig V, Longair M, Pietzsch T, Preibisch S, Rueden C, Saalfeld S, Schmid B, et al. 2012. Fiji: an open-source platform for biological-image analysis. *Nat Methods* **9:** 676–682. doi:10.1038/nmeth.2019

Smith S, Stillman B. 1989. Purification and characterization of CAF-I, a human cell factor required for chromatin assembly during DNA replication in vitro. *Cell* **58:** 15–25. doi:10.1016/0092-8674(89)90398-X

Sugie K, Funaya S, Kawamura M, Nakamura T, Suzuki MG, Aoki F. 2020. Expression of Dux family genes in early preimplantation embryos. *Sci Rep* **10:** 19396. doi:10.1038/s41598-020-76538-9

Teves SS, Weber CM, Henikoff S. 2014. Transcribing through the nucleosome. *Trends Biochem Sci* **39:** 577–586. doi:10.1016/j.tibs.2014.10.004

Valouev A, Johnson SM, Boyd SD, Smith CL, Fire AZ, Sidow A. 2011. Determinants of nucleosome organization in primary human cells. *Nature* **474:** 516–520. doi:10.1038/nature10002

Verheul TCJ, van Hijfte L, Perenthaler E, Barakat TS. 2020. The Why of YY1: mechanisms of transcriptional regulation by Yin Yang 1. *Front Cell Dev Biol* **8:** 592164. doi:10.3389/fcell.2020.592164

Voong LN, Xi L, Sebeson AC, Xiong B, Wang JP, Wang X. 2016. Insights into nucleosome organization in mouse embryonic stem cells through chemical mapping. *Cell* **167:** 1555–1570.e15. doi:10.1016/j.cell.2016.10.049

Wang J, Zhuang J, Iyer S, Lin X, Whitfield TW, Greven MC, Pierce BG, Dong X, Kundaje A, Cheng Y, et al. 2012. Sequence features and chromatin structure around the genomic regions bound by 119 human transcription factors. *Genome Res* **22:** 1798–1812. doi:10.1101/gr.139105.112

Wang C, Liu X, Gao Y, Yang L, Li C, Liu W, Chen C, Kou X, Zhao Y, Chen J, et al. 2018a. Reprogramming of H3K9me3-dependent heterochromatin during mammalian embryo development. *Nat Cell Biol* **20:** 620–631. doi:10.1038/s41556-018-0093-4

Wang J, Wu X, Wei C, Huang X, Ma Q, Huang X, Faiola F, Guallar D, Fidalgo M, Huang T, et al. 2018b. YY1 positively regulates transcription by targeting promoters and super-enhancers through the BAF complex in embryonic stem cells. *Stem Cell Reports* **10:** 1324–1339. doi:10.1016/j.stemcr.2018.02.004

Wang C, Chen C, Liu X, Li C, Wu Q, Chen X, Yang L, Kou X, Zhao Y, Wang H, et al. 2022a. Dynamic nucleosome organization

after fertilization reveals regulatory factors for mouse zygotic genome activation. *Cell Res* **32:** 801–813. doi:10.1038/s41422-022-00652-8

Wang M, Chen Z, Zhang Y. 2022b. CBP/p300 and HDAC activities regulate H3K27 acetylation dynamics and zygotic genome activation in mouse preimplantation embryos. *EMBO J* **41:** e112012. doi:10.15252/embj.202211 2012

Weintraub AS, Li CH, Zamudio AV, Sigova AA, Hannett NM, Day DS, Abraham BJ, Cohen MA, Nabet B, Buckley DL, et al. 2017. YY1 is a structural regulator of enhancer-promoter loops. *Cell* **171:** 1573–1588.e28. doi:10.1016/j.cell.2017.11 .008

Wu J, Huang B, Chen H, Yin Q, Liu Y, Xiang Y, Zhang B, Liu B, Wang Q, Xia W, et al. 2016. The landscape of accessible chromatin in mammalian preimplantation embryos. *Nature* **534:** 652–657. doi:10.1038/nature18606

Xia W, Xie W. 2020. Rebooting the epigenomes during mammalian early embryogenesis. *Stem Cell Reports* **15:** 1158–1175. doi:10.1016/j.stemcr.2020.09.005

Xu R, Li C, Liu X, Gao S. 2021. Insights into epigenetic patterns in mammalian early embryos. *Protein Cell* **12:** 7–28. doi:10 .1007/s13238-020-00757-z

Zaret KS, Mango SE. 2016. Pioneer transcription factors, chromatin dynamics, and cell fate control. *Curr Opin Genet Dev* **37:** 76–81. doi:10.1016/j.gde.2015.12.003

Zhang Y, Liu T, Meyer CA, Eeckhoute J, Johnson DS, Bernstein BE, Nusbaum C, Myers RM, Brown M, Li W, et al. 2008. Model-based analysis of ChIP-seq (MACS). *Genome Biol* **9:** R137. doi:10.1186/gb-2008-9-9-r137

Zhang B, Zheng H, Huang B, Li W, Xiang Y, Peng X, Ming J, Wu X, Zhang Y, Xu Q, et al. 2016. Allelic reprogramming of the histone modification H3K4me3 in early mammalian development. *Nature* **537:** 553–557. doi:10.1038/nature19361